

1 **Assimilation of Himawari-8 Imager Radiance Data with the WRF-3DVAR**
2 **system for the prediction of Typhoon Soulder**

3 **Dongmei Xu^{1,2,3}, Feifei Shen^{1,2,3*}, Jinzhong Min¹, Hong Li⁴, Aiqing Shu¹**

4
5 *1. The Key Laboratory of Meteorological Disaster, Ministry of Education*
6 *(KLME)/Joint International Research Laboratory of Climate and Environment*
7 *Change (ILCEC)/Collaborative Innovation Center on Forecast and Evaluation of*
8 *Meteorological Disasters (CIC-FEMD), Nanjing University of Information Science &*
9 *Technology, Nanjing 210044, China*

10 *2. Heavy Rain and Drought-Flood Disasters in Plateau and Basin Key Laboratory*
11 *of Sichuan Province, Chengdu, China*

12 *3. The Institute of Atmospheric Environment, China Meteorological Administration,*
13 *Shenyang 110000, China*

14 *4. Shanghai Typhoon Institute, China Meteorological Administration, Shanghai*
15 *200030, China*

19 **Abstract**

20 Himawari-8 is a new generation geostationary meteorological satellite launched
21 by Japan Meteorological Agency (JMA). It carries the Advanced Himawari Imager
22 (AHI) onboard, which can continuously monitor high-impact weather events with
23 high frequency space and time. The assimilation of AHI radiance data was
24 implemented with the three-dimensional variational data assimilation system of
25 Weather Research and Forecasting model (WRF-3DVAR) for the analysis and
26 prediction of Typhoon Soudelor (2015) in the Pacific Typhoon season. The effective
27 assimilation of AHI radiance data in improving the forecast of the tropical cyclone
28 during its rapid intensification has been realized. The results show that after
29 assimilating the AHI radiance data under clear sky conditions, the typhoon position in
30 the background field of the model is effectively corrected compared with the control
31 experiment without AHI radiance data assimilation. It is found that the assimilation of
32 AHI radiance data is able to improve the analyses of the water vapor and wind in
33 typhoon inner-core region. The analyses and forecasts of the minimum sea level
34 pressure, the maximum surface wind, and the track of the typhoon are further
35 improved.

36 **Key words:** Weather Research and Forecasting model; Three-Dimensional
37 Variational Data Assimilation; AHI Radiance Data; Typhoon

38

39 **1. Introduction**

40 In recent years, although researchers have made great progress in the field of
41 numerical weather prediction (NWP), the huge challenges are encountered in the
42 accurate forecasts of tropical cyclones (TCs) with rapid intensifications (DeMaria et
43 al., 2014). The predictability of these TCs is limited because it entails complex
44 multi-scale dynamic interactions (Minamide and Zhang 2018). These interactions
45 include environmental airflows, TC vortex interactions, atmosphere-ocean
46 interactions, and the effects of mesoscale and micro-convective scale, together with
47 the microphysics and atmospheric radiation. In order to attain a better initial condition
48 and improve the accuracy of the forecast, data assimilation seeks to fully utilize the
49 observations. The life span of most TCs is over the ocean where conventional
50 observations are relatively insufficient compared to the land. Therefore, by analyzing
51 observed data from satellites and planes over the ocean, it is crucial to adopt effective
52 data assimilation (DA) methods to improve the analysis and forecast of TCs.

53 With the rapid development of atmospheric radiative transfer model, many
54 numerical weather prediction centers have adopted variational DA method to
55 assimilate a variety of radiance data from different satellite observation instruments
56 (Bauer et al., 2011; Buehner et al., 2016; Derber et al., 1998; Hilton et al., 2009;
57 Kazumori et al., 2014; McNally et al., 2006; Prunet et al., 2000; Pennie, 2010). These
58 data can take up 90% of all data used in global DA system and can improve the
59 accuracy of the numerical model results strikingly (Bauer et al., 2010). Some

60 researches demonstrated that in global model, satellite radiance DA makes more
61 contribution to improving the accuracy of the numerical model results than
62 conventional observation DA does (Zapotocny et al., 2007).

63 Generally speaking, radiance data are derived from microwave and infrared
64 detecting instruments, which are from polar-orbit satellites and geostationary satellites,
65 respectively. Polar-orbit satellites cover the sphere of all the earth, thereby suitable for
66 global NWP models (Jung et al., 2008). Besides, they have finer resolutions compared
67 to geostationary satellites (Li et al., 2017; Shen et al., 2015; Xu et al., 2013). However,
68 it is highlighted that they are not able to perform continuous monitoring over a fixed
69 area, thus leaving out some rapidly intensified TCs or storms. On the contrary,
70 because geostationary satellites have a fixed location related to the earth's surface,
71 although their resolutions are lower than that of polar-orbit satellites, they can capture
72 the formation and development of mesoscale convective systems by continuous
73 monitoring (Montmerle et al., 2007; Stengel et al., 2009; Zou et al., 2011).

74 Geostationary satellites are able to continuously detect a region at a higher
75 frequency, thus observing TCs over the vast ocean effectively. In fact, they can
76 capture convective spiral cloud systems relating to TCs. As the first new generational
77 geostationary satellite, Himawari-8 plays a pioneering role for the geosynchronous
78 imagers to be launched in US, China, Korea and Europe. It has an advanced imager
79 called Advanced Himawari Imager (AHI) with 16 visible and infrared bands,
80 including 3 moisture channels, which can conduct a full-disk scan every 10 minutes.

81 Meanwhile, it can also acquire regional scanning images and that is to say it can scan
82 the Japan and the target areas every 2.5 minutes. Compared to the early
83 geosynchronous imagers, AHI has more spectrum bands and this can monitor the state
84 of atmosphere with a higher frequency.

85 In recent years, some experts and scholars have carried out some studies on the
86 data assimilation of geostationary satellite observations. Firstly utilizing GSI
87 (Gridpoint Statistical Interpolation) from NCEP (National Centers for Environmental
88 Prediction), Zou, et al (2011) conducted direct assimilation on imagers' data from
89 GOES-11 and GOES-12 to estimate their potential influences on QPF (quantitative
90 precipitation forecasts) of coastal regions in the eastern part of American. They found
91 that assimilating radiance data from GOES's imager has a remarkable improvement
92 on 6 to 12 hour's QPF near northern Mexico Gulf coast. Their work was continued by
93 Qin, et al (2013), which put thinned radiance data into GSI system to make a
94 comprehensive investigation on the issue on combined assimilation of GOES Imager
95 data together with AMSU-A (Advance Microwave Sounding Unit-A), AMSU-B
96 (Advance Microwave Sounding Unit-B), AIRS (Atmospheric Infrared Sounder),
97 MHS (Microwave Humidity Sounder), HIRS (High Resolution Infrared Radiation
98 Sounder), GSN (GOES Sounder). The results showed the effect of single assimilation
99 of AHI radiance data are better than combined assimilation in term of precipitation
100 forecast. Zou, et al (2015) adopted the GSI system to assimilate radiance data from
101 four infrared channels on GOES-13/15 and set up two experiments for comparison. A

102 symmetric vortex was used for initialization in the first experiment and an asymmetric
103 counterpart for the other experiment. Results showed that direct assimilation of
104 GOES-13/15's radiance data could yield positive effects on the track and intensity
105 forecasts of hurricane "Debbie". As the new instrument of himawari-8, there are few
106 studies on the DA of himawari-8 data. Ma, et al (2017) used 4DEnVar
107 (four-dimensional ensemble variational) DA in NCEP's GSI system to assimilate
108 radiance of three moisture channels of AHI radiance data under clear-sky condition
109 and then NCEP GFS (Global Forecast System) was utilized to estimate the impacts of
110 AHI radiance data assimilation on whether forecast. They found it had a positive
111 impact on the forecast of global vapor at high level of troposphere. Wang, et al (2018)
112 investigated the impact of assimilating three water vapor channels under clear sky on
113 the analysis and forecast of a rainstorm in Northern China with the 3DVAR method. It
114 pointed out that the assimilation of AHI radiance data could improve the wind and
115 vapor fields and the accuracy of rainfall forecast in the first 6 hours lead time.

116 Although previous researches have made several achievements in satellite data
117 assimilation and application, it is still a challenge to make more effective use of the
118 new generational geostationary satellite imager data with high spatial and temporal
119 resolution. In most of the previous studies, researches usually use a 6 hour's or even
120 longer time interval with a coarse spatial resolution. Therefore, the rapid updating
121 assimilation techniques of the geostationary satellite radiance data have not been well
122 carried out at convective scale. This study intends to build a data assimilation system

123 aiming at AHI radiance data based on the new generational mesoscale Weather
124 Research and Forecasting (WRF) model. A case of Typhoon Soudelor is studied by
125 performing numerical simulation to address the impacts of convective DA on the
126 improvement of the initial conditions of TC and the enhancement of track and
127 intensity forecasts. Our study focuses mainly on assimilating the three water vapor
128 channels (6.2, 6.9, and 7.3 μ m) since they are very sensitive to the humidity in the
129 middle and upper troposphere and have a certain effect on the lower troposphere.
130 Thus, a large amount of effective atmospheric information can be provided for AHI
131 radiance data assimilation in the troposphere. The weighting functions for the three
132 channels are provided in Fig. 1.

133 Section 2 describes the observations and the data assimilation system. Introductions
134 to the typhoon case and the experimental setup are provided in section 3. The detailed
135 results in terms of the analyses and the forecasts are illustrated in section 4 before
136 conclusions are summarized in section 5.

137 **2. Observational data and DA system**

138 *2.1 An introduction to Himawari-8 AHI radiance data*

139 Himawari-8 satellite was launched by JMA to a geosynchronous orbit on 17
140 October 2014 and has begun its operational use since 7 July 2015 (Bessho et al.,
141 2016). It is located between the equator and 140.7°E, thus the earth is observed
142 between 60°N and 60°S meridionally and between 80°E and 160°W zonally.
143 Compared to its previous generation Himawari-7, its detective ability can get

144 significantly improved since the instrument AHI on Himawari-8. Besides, its device is
145 comparable to imagers on American GOES-R satellite (Goodman et al., 2012; Schmit
146 et al., 2005; Schmit et al., 2008; Schmit et al., 2017). AHI is able to provide a full-disk
147 image every 10 minutes and complete a scan over Japan every 2.5 minutes. AHI
148 conducts continuous scan and detection on a moving targeted typhoon. It has 16
149 channels covering visible, near-infrared, and infrared spectral bands with a resolution
150 of 0.5 km or 1 km, and 2 km respectively. Channel 8 to 10 (6.2, 6.9, and 7.3 μm) are
151 water vapor bands that are sensitive to the humidity in the middle and upper
152 troposphere (Di et al., 2016). Other channels (channel 11, 12, 16: 8.6 μm , 9.6 μm , and
153 13.3 μm) are either monitoring other fields such as the thin ice clouds, volcanic SO₂
154 gas, the ozone or CO₂, or the atmospheric window channels (13-15: 10.4, 11.2, and
155 12.4 μm) function as monitors for ice crystal/water, low water vapor, volcanic ash, sea
156 surface temperature and other phenomena (Bessho et al., 2016).

157 *2.2 WRFDA system and AHI radiance data*

158 WRFDA system is designed by National Center for Atmospheric Research
159 (NCAR) and it contains 3DVAR, 4DVAR, Hybrid parts. This research is based on the
160 3DVAR method. An interface that is suitable for AHI DA is built in WRFDA system.
161 Currently, WRFDA is able to assimilate many conventional and unconventional
162 observations. In terms of satellite radiance data, this system is compatible with
163 RTTOV (the Radiative Transfer model of the Television and Infrared Observational
164 Satellite Operational Vertical sounder) and CRTM (Community Radiative Transfer

165 Model, Liu and Weng, 2006) as observation operators. In this study, CRTM is utilized
 166 as the observation operator to simulate and compute AHI radiance data. Estimating
 167 the systematic bias and random error of the observations caused by the errors of
 168 numerical models and instruments are the key factors to directly assimilate the
 169 satellite radiance data. Apart from eliminating cloud pixels, other procedures for
 170 quality control are as follows. (1) when reading the data, remove the observed outliers
 171 with values below 50 K or above 550 K; (2) only the marine observations are applied
 172 by removing the observations on the land and the observations over complex surfaces;
 173 (3) remove observations when the observation minus the background is larger than 3
 174 times of the observation error; (4) the pixels are removed when the cloud liquid water
 175 path calculated by the background field of the numerical model is greater than or
 176 equal to 0.2 kg/m²; (5) eliminate the data when the observation minus background is
 177 greater than 5 K.

178 By using 3DVAR algorithm, the assumption is that there is no bias between
 179 observation and background (Dee et al., 2009; Liu et al., 2012; Zhu et al., 2014). A
 180 bias correction scheme for observation is essential before DA. Usually, radiance bias
 181 can be obtained by a linear combination of a set of forward operators.

$$182 \quad \tilde{H}(x, \beta) = H(x) + \beta_0 + \sum_{i=1}^{N_p} \beta_i p_i \quad (1)$$

183 Here, $H(x)$ represents the initial observation operator (before the bias
 184 correction), x represents the mode state vector, β_0 represents a constant component

185 of the total bias (constant part), P_i and β_i represent the i -th predictor and its
186 coefficient respectively. In this study, four potentially state-dependent predictors
187 (1000–300 hPa and 200–50 hPa layer thicknesses, surface skin temperature, and total
188 column water vapor) are applied. The variational bias correction (VarBC) scheme is
189 utilized to update the bias correction coefficient variationally with the new
190 observation operator considered in the cost function of 3DVAR.

191 **3. Introduction to the typhoon and experimental design**

192 *3.1 Typhoon Soudelor*

193 From the record of the China Meteorological Administration (CMA), Typhoon
194 Soudelor was the 13th typhoon in 2015 as the second strongest tropical cyclone in that
195 year. At 1200 UTC 30 July 2015, it formed at northwest Pacific Ocean as a tropical
196 storm at 13.6° N, 159.2° E, then moved north-westwards. It upgraded to a strong
197 tropical storm at 2100 UTC 1 August 2015. Afterwards, it went through a process of
198 rapid intensification. It became a typhoon at 0900 UTC 2 August 2015, a strong
199 typhoon at 2100 UTC 2 August 2015, a super typhoon at 0900 UTC 3 August 2015.
200 Then it weakened to a strong typhoon in the morning on 5 August 2015. However, it
201 intensified to a super typhoon again at 1200 UTC 7 August 2015 with a maximum
202 surface wind of 52 m s^{-1} , moving west by north, and its intensity raised to its second
203 peak. It was reduced to a strong typhoon again at 1800 UTC 7 August 2015. It
204 decreased to a typhoon, entering to Taiwan Strait. It landed again as a typhoon at 1410
205 UTC on the coast of Fujian Province, China. Owing to continuous orographic friction,

206 it decreased to a tropical depression. Fig. 2 shows the track of Soudelor and different
207 color lines represent typhoon's maximum surface wind. It is displayed that after the
208 formation of typhoon, its track is relatively stable. After July 30, the tropical
209 depression moved west by north at a speed of about 20 km/h. Its moving tendency
210 changed slightly within 10 days of its generation. However, its intensity went through
211 a rapid intensification, a weakening, a second intensification, then a continuous
212 weakening till disappearing gradually after landing on the China. Fig. 3 demonstrates
213 the variation of typhoon's intensity from 31 July 2015 to 5 August 2015. It is shown
214 that typhoon's maximum surface wind increased fast, while its minimum sea level
215 pressure decreased sharply. This was the stage of typhoon's rapid intensification. The
216 date from 1 August 2015 to 3 August 2015 during its rapid intensification are selected
217 as a research object.

218 *3.2 Experimental design*

219 Two experiments are designed to investigate the effects of AHI radiance data
220 direct assimilation on the analysis and forecast of Typhoon Soudelor starting from
221 1800 UTC 1 August 2015 to 0000 UTC 3 August 2015. WRF 3.9.1 is employed as the
222 forecast model in this experiment. Arakawa C grid is used in the horizon with a 5 km
223 grid distance. As is known, Arakawa A grid is "unstaggered" by evaluating all
224 quantities at the same point on each grid cell. The "staggered" Arakawa B-grid
225 separates the evaluation of the velocities at the grid center and masses at grid corners.
226 Arakawa C grid further separates evaluation of vector quantities compared to the

227 Arakawa B-grid. Vertically, it has 41 eta levels using 10 hPa as its top with coarser
228 vertical spacing for the higher levels. Model center is (17.5 °N, 140 °E) (Fig. 4). The
229 initial condition and lateral boundary are provided by 0.5°×0.5° Global Forecasting
230 System (GFS) reanalysis data. The following parameterization schemes are used: The
231 following parameterization schemes are used: WDM6 microphysics scheme (Lim et
232 al., 2010), Grell Devenyi cumulus parameterization scheme (Grell et al., 2002),
233 RRTM (Rapid Radiative Transfer Model) longwave radiation scheme (Mlawer et al.,
234 1997), shortwave radiation scheme (Dudhia et al., 1989), and YSU boundary layer
235 scheme (Hong et al., 2006) .

236 The experimental procedures are illustrated by Fig. 5. Firstly, a 6 hour's spin-up
237 conducted initialized from 1800 UTC 1 August 2015 to prepare the background field
238 for the data assimilation at 0000 UTC 2 August 2015. The first experiment is
239 assimilating GTS (Global Telecommunications System) conventional data (including
240 aircraft report, ship report, sounding report, satellite cloud wind data, ground station
241 data) only, which is called control experiment (CTNL). Another experiment is
242 configured with AHI radiance data assimilation (AHI_DA). AHI radiance data is
243 assimilated hourly further from 0000 UTC to 0600 UTC on 2 August 2015.
244 Afterwards, an 48 hours forecast is launched as the deterministic forecast. The
245 climatological background error (BE) statistics are estimated using the National
246 Meteorological Center (NMC) method. There are 5 control variables applied in this
247 study including U component, V component, full temperature, full surface pressure,

248 and pseudo-relative humidity. The observation error for each channel is estimated
249 based on the observed brightness temperature minus background brightness
250 temperature (OMB) from 0000 UTC on 1 August 2015 to 0000 UTC on 3 August
251 2015 every 6 hours.

252 Fig. 4 also shows the distribution of GTS observation data at the simulated
253 domain at 0000 UTC 2 August 2015. It is proved that raw radiance observations
254 thinned to a grid with 2–6 times of the model grid resolution are able to remove the
255 potential error correlations between adjacent observations (Schwartz et
256 al., 2012; Xu et al., 2015; Choi et al., 2017). Hence, 20 km is chosen to make
257 thinning of AHI radiance data. Also, sensitivity experiments with 25 km, and 30 km
258 thinning mesh are also conducted with similar results. The length scale and the
259 variance scale are set to be 0.5 and 1 respectively after several sensitivity experiments
260 conducted on tuning the background error. Similar conclusions are also found in Shen
261 and Min (2015) with the scale factors related to the static background error
262 covariance.

263 **4. Results**

264 *4.1 Minimization iterations*

265 Fig. 6 shows the cost function and gradient with the iteration times. There is an
266 obvious exponential decrease curve in Fig. 6a, while Fig. 6b shows gradient decreases
267 with the increase of iteration times. Taking Fig. 6a as an example, cost function
268 decreases remarkably in the first 10 iterations. However, after 30 times of iteration,

269 the cost function curve becomes smooth gradually. The differences between
270 background field and observation are largest. With continuous iterations, background
271 field goes through continued adjustments. Finally, the cost function tends to reach a
272 stable minimum that represents the point when cost function has its optimal solution.
273 Besides, the gradient in Fig. 6b decreases stably with increasing iterations. The
274 exponential decrease of the cost function and the change trend of its gradient indicate
275 that the effectiveness of AHI radiance DA. The final iterated analytical field is close
276 to the observation.

277 *4.2 Analytical results of the brightness temperature*

278 Fig. 7a, c, e show the distribution of OMB, while the observed brightness
279 temperature minus analytical brightness temperature (OMA) after the bias correction
280 of AHI radiance data are presented in Fig. 7b, d, f from channel 8, 9, and 10 at 0000
281 UTC 2 August 2015. It should be pointed that even only parts of the AHI radiance
282 data are applied after quality control in the data assimilation, the radiative transfer
283 model is able to simulate the brightness temperature for all the pixels with the
284 background and the analysis respectively for the verification purpose. The similar
285 verification method is also applied in Yang et al., (2016). In the Fig. 7a, part of
286 typhoon's spiral cloud belt is clearly visible. The brightness temperature in typhoon's
287 inner-core area is low, while the brightness temperature in other areas is high. The
288 mean of observed OMB was -4.65 K, indicating that the background brightness
289 temperature is higher than the observation. It is found in Fig. 7b that the OMA values

290 of most pixels are below 0.02 K, indicating that the analytical field fitting the
291 observation after analyzing. It can be inferred from Fig. 7a, c, and e that the
292 magnitude in OMB of channel 10 is generally larger than that of channel 9, while that
293 of the OMB in channel 8 is the smallest. This is because the detection height of
294 channel 10 is lower than that of channel 8 and 9 seen from the weighting function (Fig.
295 1), indicating channel 10 is largely affected by the clouds. Conversely, the weighting
296 peak of the channel 8 is the highest, being least affected by the clouds. In general, the
297 analytical brightness temperature match well with the observed brightness
298 temperature of all the three water vapor channels after the assimilation of AHI
299 radiance data.

300 Fig. 8 shows the effect of the bias correction for AHI radiance data at 0000 UTC
301 2 August 2015. Fig. 8a, d, g show the scatter plots of the observed brightness
302 temperature and the brightness temperature from the background before the bias
303 correction. Fig. 8b, e, h show results after bias correction. Fig. 8c, f, i show the scatter
304 plots of observed brightness temperature and analytical brightness temperature after
305 bias correction. From Fig. 8a, before the bias correction, the values from the
306 observation and the background are comparable, but most of the scatter points are
307 below the diagonal line. This suggests that the observed brightness temperature is
308 higher than the background simulated brightness temperature. From Fig. 8b, after the
309 bias correction, observed warm bias is corrected to some extent. From Fig. 8a, b, after
310 the bias correction, the root mean square error (RMSE) of OMB decreases from 1.864

311 K to 1.627 K, with the average decreasing from 0.956 K to 0.358 K, proving the
312 validity and rationality of the variational bias correction. Compared to the result of
313 Fig. 8b, the scatters in Fig. 8c are more symmetrical, fitting closely to the diagonal
314 line. The mean and RMSE were also significantly reduced, suggesting that the
315 analytical field is more similar to observation than background field. Channel 9, 10
316 have a similar result, but with a significantly reduced mean and RMSE, indicating that
317 the background field and analytical field of channel 9, 10 match better with the
318 observation than channel 8 does. Among them the RMSE of channel 10 is smallest as
319 0.234 K in Fig. 8i, which is likely related to strict cloud detection scheme for channel
320 10 with rather lower detecting peak (Wang et al., 2018).

321 Fig. 9 shows the observation numbers, the mean, and the standard deviation of
322 OMB and OMA of channel 8, 9, and 10 before and after the bias correction. It can be
323 seen that after the quality control, 24057, 24181, 21785 observations are adopted in
324 the DA system for channel 8, 9, and 10, respectively. From the mean value of OMB
325 before the bias correction, the value of the three channels is relatively small,
326 indicating that the simulated brightness temperature of the three channels is close to
327 the observed brightness temperature. The lowest mean of 0.3 K is found in channel 10,
328 indicating that the simulated brightness temperature of channel 10 is closest to the
329 observed brightness temperature. Bias correction effectively corrects the systematic
330 bias and reduces the mean value of observation residuals. After the bias correction,
331 the OMB mean value of the three channels significantly decreases to nearly 0 K. With

332 the bias correction, the simulated brightness temperature is almost the same as the
333 observed brightness temperature. The analysis of the standard deviation of OMB
334 shows that the results are comparable before and after the bias correction. The
335 standard deviation of OMA decreases by about 80% compared to OMB, indicating
336 that the analyses fit better with the observations after the data assimilation.
337 Differences between the standard deviations of the OMB and OMA were statistically
338 significant at the 95% level using zero difference for the null hypothesis.

339 The RMSEs of the simulated brightness temperature by the NWP model before
340 and after the assimilation are also calculated against the AHI radiance observations.
341 Fig. 10 shows the RMSEs during the DA cycles for channels 8, 9, 10. As can be seen
342 from Fig. 10, RMSE decreases after each analysis in AHI_DA. The most significant
343 improvement is from the first analysis cycle of channel 8, where RMSE of the
344 brightness temperature after assimilation significantly decreases from 1.64 K to 0.46
345 K, possibly due to the largest adjustment on the background for the first analysis time.
346 The background before the assimilation is the short-term forecast from the previous
347 analysis. The increase of the RMSE in the fluctuation arise from the model error in
348 the 1 hour short-term forecast. Overall, the effect of the analysis from the channel 10
349 is most significant.

350 *4.3 Analysis of the typhoon structure*

351 Fig. 11 shows the wind field at sea level and the distribution of water vapor at
352 850 hPa at 0000 UTC 2 August 2015. The obvious cyclonic eddy circulation

353 structures in the core area of the typhoon are found in both fields, while the
354 anti-cyclonic circulation exists in the northwest quadrant of the typhoon. The mixing
355 ratio of water vapor in the region where the typhoon located is very high and the wind
356 field is cyclonic, indicating that the typhoon has a continuous water vapor advection.
357 This contributes to the enhancement of typhoon (Kamineni, et al., 2003). From the
358 flow field of the control experiment in Fig. 11a, the water vapor convergence in the
359 center of the typhoon region is weak with the low intensity and smaller coverage. As
360 can be seen from Fig. 11b, after the assimilation of AHI radiance data, the streamlines
361 in the typhoon region become denser, indicating that the cyclonic circulation is
362 strengthened. Conversely, the intensity and distribution of the water vapor after the
363 assimilation of AHI radiance data tend to contribute to the developing typhoon. This
364 suggests that the assimilation of AHI radiance data are able to significantly improve
365 the large-scale environmental field in the simulation region of Typhoon Soudelor. It
366 should be pointed out that the model status in the cloudy area are modified due to the
367 spatial correlation in the background error covariance. The similar findings for
368 small-scale information in the cloudy area can also be referred in Wang et al., (2018).

369 *4.4 Track forecast*

370 In order to further evaluate the effect of AHI radiance data assimilation, a 48-hour
371 deterministic forecast is launched with the analyses initialized from 0000 UTC 2
372 August 2015 and 0600 UTC 2 August 2015 respectively. The best track data are
373 provided by the CMA (Yu et al., 2007; Song et al., 2010). As can be seen in Fig. 12a,

374 at the beginning of the forecast, the initial location of the typhoon from the CTNL
375 experiment has large south bias and east bias at 0000 UTC and 0600 UTC
376 respectively. Conversely, the location of the typhoon in AHI_DA is relatively closer to
377 the observation at the beginning. During the following few hours of forecasts, the
378 typhoon track predicted by the CTNL continues to show a south-west bias with the
379 environmental wind, while the track predicted by AHI_DA match better with the best
380 track. Fig. 12c shows the averaged typhoon track error over the two forecasts
381 predicted by the two experiments. At the initial time of the forecast, the track errors of
382 CTNL and AHI_DA are significantly different, with the magnitude of 55.6 km and
383 13.4 km, respectively. During the subsequent 48-hour forecast, the track error of the
384 CTNL gradually increases with the forecast time reaching 167.1 km at the end of the
385 forecast. In contrast, the track error of AHI_DA is consistently less than 122.5 km
386 during the 48-hour forecast period. In general, the average track error of the CTNL is
387 168.57 km, and the average track error of AHI_DA experiment is only 67.0 km,
388 indicating a significant improvement in the track prediction.

389 Fig. 13 provides the time series of the typhoon intensity from the two
390 experiments in terms of the averaged maximum surface wind and minimum sea level
391 pressure error over the two forecasts initialized from 0000 UTC 2 August 2015 and
392 0600 UTC 2 August 2015 respectively. It can be seen that the maximum surface wind
393 error predicted by the AHI_DA is much lower than that by the CTNL, due to the
394 overall under estimation for the strength of Typhoon Soudelor simulated in the

395 background field. The maximum surface wind predicted by AHI_DA fit closer to the
396 best track data with the maximum difference about 2.6 m s^{-1} after 12 hours forecast .
397 In Fig. 13b, the results of the minimum sea level pressure are consistent with Fig. 13a.

398 **5. Conclusion**

399 An interface for AHI radiance data assimilation on the WRFDA system based on
400 the 3DVAR assimilation method was built. Based on the Typhoon Soudelor in 2015,
401 two experiments for comparison was designed to examine the impact of AHI water
402 vapor channel radiance data assimilation on the analysis and prediction of the rapid
403 development stage of Typhoon Soudelor under clear sky condition. Following
404 conclusions are obtained:

405 (1) The AHI radiance data on the new generation of geostationary meteorological
406 satellite is able to reflect the structure of Typhoon Soudelor very clearly. After a series
407 of pre-procedures such as the quality control, the bias correction, cloudy pixels are
408 able to effectively be eliminated, ensuring the validity and rationality of the Ahi
409 radiance data. The biases are also eliminated from the VarBC statistical method,
410 which is able to provide a positive impact on the data assimilation procedure for the
411 typhoon numerical simulation.

412 (2) Compared with the control experiment with only GTS data, the 3DVAR
413 assimilation including AHI radiance data is able to improve the structure of typhoon's
414 core and outer rain band. Also, the position and intensity of typhoon in the
415 background field are able to be corrected.

416 (3) It is found that the track, maximum surface wind, and minimum sea level pressure
417 from the AHI radiance data assimilation experiment match better with the best track
418 than the control experiment does for the subsequent 18-hour forecast.

419 In this study, the AHI water radiance data assimilation is conducted under the
420 clear sky condition. The results of the experiments indicate that AHI radiance data
421 assimilation has a positive effect on the analysis and prediction of rapidly intensifying
422 TC. Considering the complex influence of underlying surface, only the rapid
423 development stage of typhoon at sea were studied, while the whole generation,
424 development and disappearance stage of typhoon can also be studied in the future. In
425 addition, based on the AHI radiance data of the water vapor channels under the
426 condition of clear sky, only 3DVAR method was adopted. Further improvements
427 under the condition of all sky and hybrid DA can be obtained in the future.

428 **Acknowledgments**

429 This research was primarily supported by the Chinese National Natural Science
430 Foundation of China (G41805016), the Natural Science Foundation of Jiangsu
431 Province (BK20170940), the Chinese National Natural Science Foundation of China
432 (G41805070), the Chinese National Key R&D Program of China (2018YFC1506404,
433 2018YFC1506603), the research project of Heavy Rain and Drought-Flood Disasters
434 in Plateau and Basin Key Laboratory of Sichuan Province in China (SZKT201901,
435 SZKT201904), the research project of the Institute of Atmospheric Environment,
436 China Meteorological Administration, Shenyang in China (2020SYIAE07,

437 2020SYIAE02).

438

439

References

440 Bauer, P., Geer, A.J., Lopez, P., and Salmond, D.: Direct 4D–Var assimilation of
441 all-sky radiance. Part I: Implementation, Quarterly Journal of the Royal
442 Meteorological Society, 136, 1868-1885, 2010.

443 Bauer, P., Auligné, T., Bell, W., Geer, A., Guidard, V., Heilliette, S., et al: Satellite
444 cloud and precipitation assimilation at operational NWP centres, Quarterly Journal of
445 the Royal Meteorological Society, 137, 1934-1951, 2011.

446 Bessho, K., Date, K., Hayashi, M., Ikeda, A., Imai, T., Inoue, H., et al.: An
447 introduction to Himawari-8/9—Japan's new-generation geostationary meteorological
448 satellites, Journal of the Meteorological Society of Japan, 94, 151-183, 2016.

449 Buehner, M., Caya, A., Carrieres, T., and Pogson, L.: Assimilation of SSMIS and
450 ASCAT data and the replacement of highly uncertain estimates in the Environment
451 Canada Regional Ice Prediction System, Quarterly Journal of the Royal
452 Meteorological Society, 142, 562-573, 2016. Choi, Y., Cha, D.-H., Lee, M.-I., Kim,
453 J., Jin, C.-S., Park, S.-H., and Joh, M.-S.: Satellite radiance data assimilation for
454 binary tropical cyclone cases over the western North Pacific, J. Adv. Model. Earth
455 Syst., 9, 832-853, 2017.

456 Dee, D.P., and Uppala, S.: Variational bias correction of satellite radiance data in the

457 ERA–Interim reanalysis, *Quarterly Journal of the Royal Meteorological Society*, 135,
458 1830-1841, 2009.

459 DeMaria, M., Sampson C.R., Knaff J.A., and Musgrave K.D.: Is tropical cyclone
460 intensity guidance improving? *Bulletin of the American Meteorological Society*, 95,
461 387-398, 2014.

462 Derber, J.C., and Wu, W.S.: The use of TOVS cloud–cleared radiance in the NCEP
463 SSI analysis system, *Mon. Wea. Rev.*, 126, 2287-2299, 1998.

464 Di, D., Ai, Y., Li, J., Shi, W., and Lu, N.: Geostationary satellite-based 6.7 μm band
465 best water vapor information layer analysis over the Tibetan Plateau, *Journal of*
466 *Geophysical Research: Atmospheres*, 121, 4600-4613, 2016.

467 Dudhia, J.: Numerical Study of Convection Observed during the Winter Monsoon
468 Experiment Using a Mesoscale Two-Dimensional Model, *Journal of the Atmospheric*
469 *Sciences*, 46, 3077-3107, 1989.

470 Goodman, S.J., Gurka, J., DeMaria, M., Schmit, T.J., Mostek, A., Jedlovec, G., et al.:
471 The GOES-R proving ground: Accelerating user readiness for the next-generation
472 geostationary environmental satellite system, *Bulletin of the American Meteorological*
473 *Society*, 93, 1029-1040, 2012.

474 Grell G.A., Dévényi D.: A generalized approach to parameterizing convection
475 combining ensemble and data assimilation techniques, *Geophys. Res. Lett.*, 29,
476 587-590, 2002.

477 Hilton, F., Atkinson, N. C., English, S. J., and Eyre, J. R.: Assimilation of IASI at the
478 Met Office and assessment of its impact through observing system experiments,
479 Quarterly Journal of the Royal Meteorological Society, 135, 495-505, 2009.

480 Hong S.Y., Noh Y., Dudhia J.: A New Vertical Diffusion Package with an Explicit
481 Treatment of Entrainment Processes. Mon. Wea. Rev, 134, 2318-2341, 2006.

482 Jung, J.A., Zapotocny, T.H., Le Marshall, J.F., and Treadon, R.E.: A two-season
483 impact study on NOAA polar-orbiting satellites in the NCEP Global Data
484 Assimilation System, Weather Forecasting, 23, 854-877, 2008.

485 Kamineni, R., Krishnamurti, T., Ferrare, R., Ismail, S., and Browell, E.: Impact of
486 high resolution water vapor cross-sectional data on hurricane forecasting, Geophysical
487 Research Letters, 30, 38-1, 2003. Kazumori, M.: Satellite radiance assimilation in the
488 JMA operational mesoscale 4DVAR system, Mon. Wea. Rev, 142, 1361-1381, 2014.

489 Li, X., and Zou, X.: Bias characterization of CrIS radiances at 399 selected channels
490 with respect to NWP model simulations, Atmospheric Research, 196, 164-181, 2017.

491 Lim, K.-S. S., and Hong, S.-Y.: Development of an effective double-moment cloud
492 microphysics scheme with prognostic cloud condensation nuclei (CCN) for weather
493 and climate models. Mon. Wea. Rev, 138, 1587-1612, 2010.

494 Liu, Z., Schwartz, C.S., Snyder, C., and Ha, S.Y.: Impact of assimilating AMSU-A
495 radiance on forecasts of 2008 Atlantic tropical cyclones initialized with a limited-area
496 ensemble Kalman filter, Mon. Wea. Rev., 140, 4017-4034, 2012.

497 Liu, Q., and Weng, F.: Advanced doubling-adding method for radiative transfer in
498 planetary atmosphere. *J. Atmos. Sci.*, 63, 3459–3465, 2006.

499 Ma, Z., Maddy E.S., Zhang B., Zhu T., and Boukabara S.A.: Impact Assessment of
500 Himawari-8 AHI Data Assimilation in NCEP GDAS/GFS with GSI, *J. Atmos.*
501 *Oceanic Technol.*, 34, 797-815, 2017.

502 McNally, A.P., Watts, P.D., Smith, J.A., Engelen, R., Kelly, G.A., Thépaut, J.N.,
503 and Matricardi, M.: The assimilation of AIRS radiance data at ECMWF, *Quarterly*
504 *Journal of the Royal Meteorological Society*, 132, 935-957, 2006.

505 Minamide, M., and Zhang F.: Assimilation of all-sky infrared radiances from
506 himawari-8 and impacts of moisture and hydrometer initialization on
507 convection-permitting tropical cyclone prediction. *Mon. Wea. Rev.*, 146, 3241-3258,
508 2018.

509 Mlawer E.J., Taubman S.J., Brown P.D., et al.: Radiative transfer for inhomogeneous
510 atmospheres: RRTM, a validated correlated-k model for the longwave, *Journal of*
511 *Geophysical Research Atmospheres*, 102, 16663-16682, 1997.

512 Montmerle, T., Rabier, F., and Fischer, C.: Relative impact of polar-orbiting and
513 geostationary satellite radiance in the Aladin/France numerical weather prediction
514 system, *Quarterly Journal of the Royal Meteorological Society*, 133, 655-671, 2007.

515 Noh Y., Cheon W.G., Hong S.Y., et al.: Improvement of the K-profile Model for the
516 Planetary Boundary Layer based on Large Eddy Simulation Data, *Boundary-Layer*

517 Meteorology, 107, 401-427, 2003.

518 Prunet, P., Thépaut, J.N., Cassé, V., Pailleux, J., Baverez, A., and Cardinali,
519 C.: Strategies for the assimilation of new satellite measurements at Météo–
520 France, *Advances in Space Research*, 25, 1073-1076, 2000.

521 Qin, Z., Zou, X., Weng, F.: Evaluating Added Benefits of Assimilating GOES Imager
522 Radiance Data in GSI for Coastal QPFs, *Mon. Wea. Rev.*, 141, 75-92, 2013.

523 Rennie, M.P.: The impact of GPS radio occultation assimilation at the Met
524 Office, *Quarterly Journal of the Royal Meteorological Society*, 136, 116-131, 2010.

525 Schmit, T.J., Gunshor, M.M., Paul Menzel, W., Gurka, J., Li, J., and Bachmeier,
526 S.: Introducing the next-generation advanced baseline imager (ABI) on
527 GOES-R, *Bulletin of the American Meteorological Society*, 86, 1079-1096, 2005.

528 Schmit, T.J., Li, J., Li, J., Feltz, W.F., Gurka, J.J., Goldberg, M.D., and Schrab,
529 K.J.: The GOES-R Advanced Baseline Imager and the continuation of current sounder
530 products, *Journal of Applied Meteorology and Climatology*, 47, 2696-2711, 2008.

531 Schmit, T.J., Griffith, P., Gunshor, M.M., Daniels, J.M., Goodman, S.J., and Lehair,
532 W.J.: A closer look at the ABI on the GOES-R series, *Bulletin of the American
533 Meteorological Society*, 98, 681-698, 2017.

534 Schwartz, C. S., Liu, Z., Chen, Y. and Huang X. - Y.: Impact of assimilating
535 microwave radiances with a limited - area ensemble data assimilation system on
536 forecasts of Typhoon Morakot, *Weather Forecasting*, 27, 424-437, 2012.

537 Shen, F., and Min, J.: Assimilating AMSU-A radiance data with the WRF hybrid
538 En3DVAR system for track predictions of Typhoon Megi (2010), *Advances in*
539 *Atmospheric Sciences*, 32, 1231-1243, 2015.

540 Song J-J, Wang Y, Wu L.: Trend discrepancies among three best track data sets of
541 western North Pacific tropical cyclones. *J. Geophys. Res.* 115: D12128, DOI:
542 10.1029/2009JD013058, 2010.

543 Stengel, M., Undén, P., Lindskog, M., Dahlgren, P., Gustafsson, N., and Bennartz, R.:
544 Assimilation of SEVIRI infrared radiance with HIRLAM 4D-Var, *Quarterly Journal*
545 *of the Royal Meteorological Society*, 135, 2100-2109, 2009.

546 Wang, Y., Liu, Z., Yang, S., Min, J., Chen, L., Chen, Y., and Zhang, T.: Added value of
547 assimilating Himawari-8 AHI water vapor radiances on analyses and forecasts for
548 “7.19” severe storm over north China, *Journal of Geophysical Research: Atmospheres*,
549 123, 3374-3394, 2018.

550 Xu, D., Liu, Z., Huang, X.-Y., Min, J., and Wang, H.: Impact of assimilation IASI
551 radiances on forecasts of two tropical cyclones, *Meteorology and Atmospheric*
552 *Physics*, 122, 1-18, 2013.

553 Xu, D., Huang X.-Y., Wang H., Mizzi, A. P. and Min J.: Impact of assimilating
554 radiances with the WRFDA ETKF/3DVAR hybrid system on prediction of two
555 typhoons in 2012, *J. Meteorol. Res*, 29, 28-40, 2015.

556 Yang, C., Liu, Z., Bresch, J., Rizvi, S. R. H, Huang, X.-Y., and Min, J.: AMSR2

557 all-sky radiance assimilation and its impact on the analysis and forecast of Hurricane
558 Sandy with a limited-area data assimilation system, *Tellus A: Dynamic Meteorology*
559 and *Oceanography*, 68, 2016.

560 Yu H, Hu C, Jiang L.: Comparison of three tropical cyclone intensity datasets. *Acta*
561 *Meteorol. Sin.* 21, 121-128, 2007.

562 Zapotocny, T.H., Jung, J.A., Le Marshall, J.F., and Treadon, R.E.: A two-season
563 impact study of satellite and in situ data in the NCEP Global Data Assimilation
564 System, *Weather Forecasting*, 22, 887-909, 2007.

565 Zhu, Y., Derber, J., Collard, A., Dee, D., Treadon, R., Gayno, G., and Jung,
566 J.A.: Enhanced radiance bias correction in the National Centers for Environmental
567 Prediction's Gridpoint Statistical Interpolation data assimilation system, *Quarterly*
568 *Journal of the Royal Meteorological Societ*, 140, 1479-1492, 2014.

569 Zou, X., Qin, Z., and Weng, F.: Improved coastal precipitation forecasts with direct
570 assimilation of GOES-11/12 imager radiance, *Mon. Wea. Rev.*, 139, 3711-3729, 2011.

571 Zou, X., Qin Z., and Zheng Y.: Improved tropical storm forecasts
572 with GOES-13/15 imager radiance assimilation and asymmetric vortex initialization
573 in HWRF, *Mon. Wea. Rev.*, 143, 2485-2505, 2015.

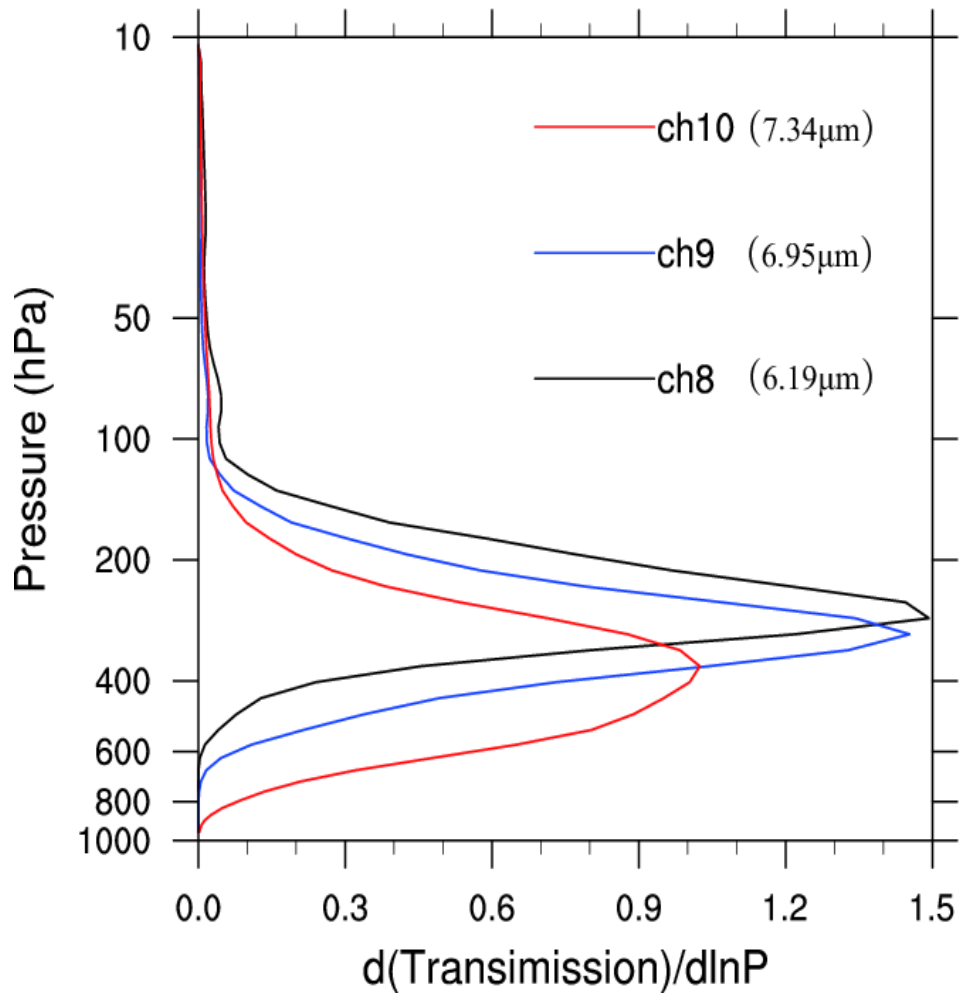
574

575

576

List of Figures

577



578

579 Fig.1 Weighting functions of Himawari-8 Advanced Himawari Imager three water

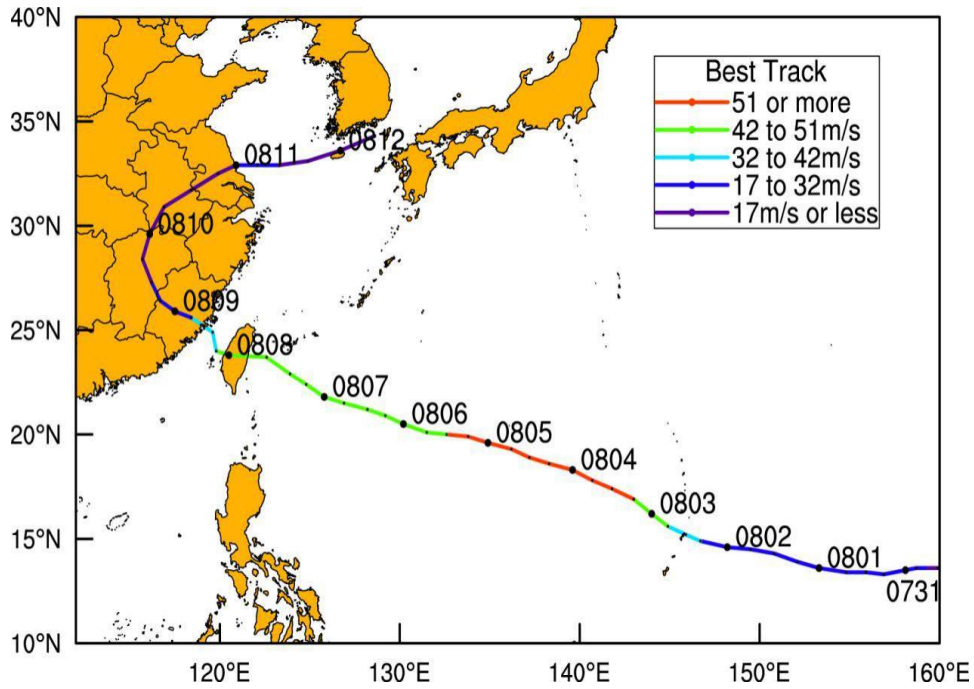
580 vapor channels for Channel 8, 9, and 10.

581

582

583

584



585

586 Fig.2 The best track of Soudelor from the China Meteorological Administration
587 (CMA) from 0000 UTC 30 July to 0600 UTC 12 August 2015. Different colors
588 represent intensity changes.

589

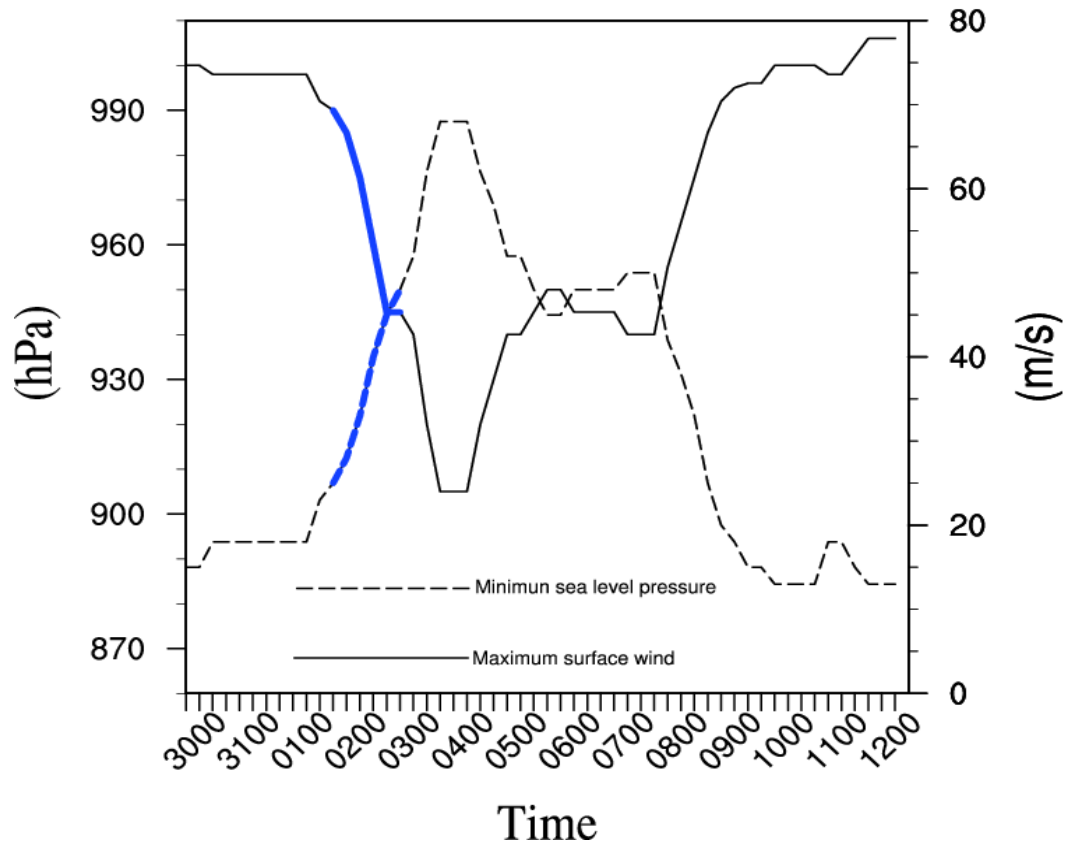
590

591

592

593

594



595

596 Fig. 3 The time series of the minimum sea level pressure (solid line, unit: hPa) and the
 597 maximum surface wind (dash line, unit: m s⁻¹) of typhoon Soudelor from the CMA
 598 best-track data.

599

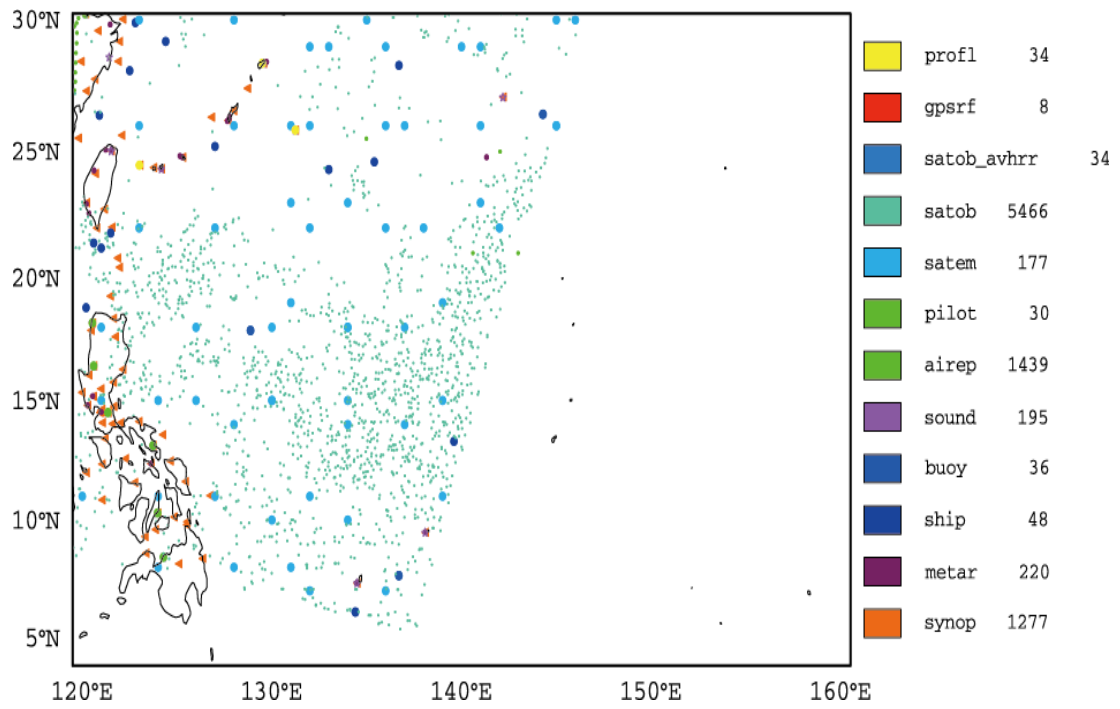
600

601

602

603

604



605

606 Fig. 4 Distribution of GTS observations in the simulated area at 0000 UTC 2 August

607 2015. On the right side of the map is the name of observation data and the number of

608 observations.

609

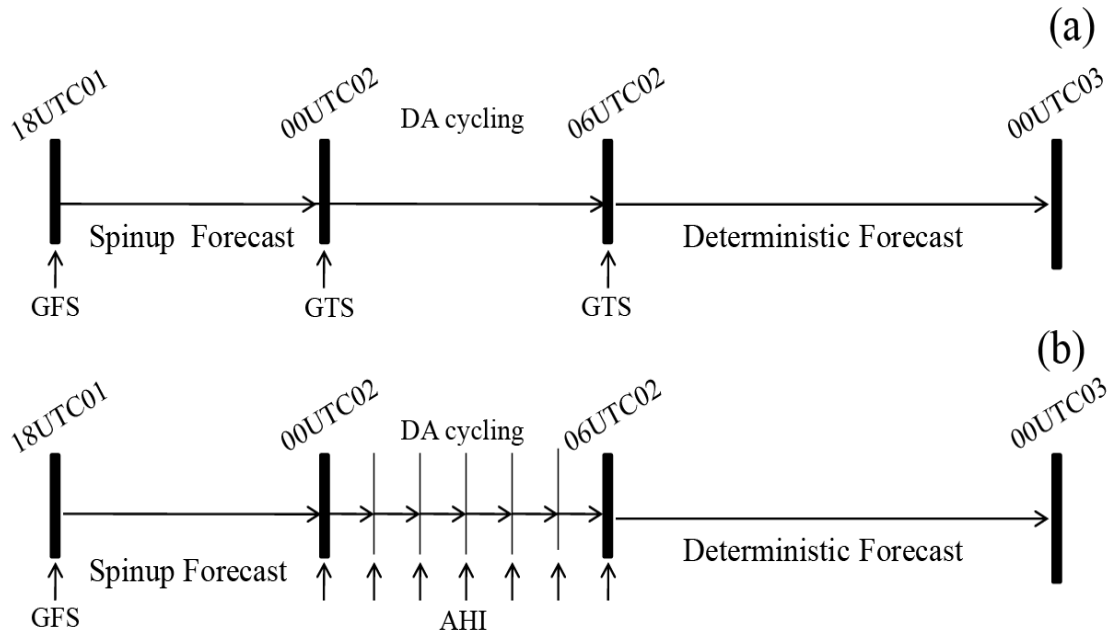
610

611

612

613

614



615

616 Fig. 5 The flow chart of the data assimilation experiments. (a) CTNL, (b) AHI_DA

617

618

619

620

621

622

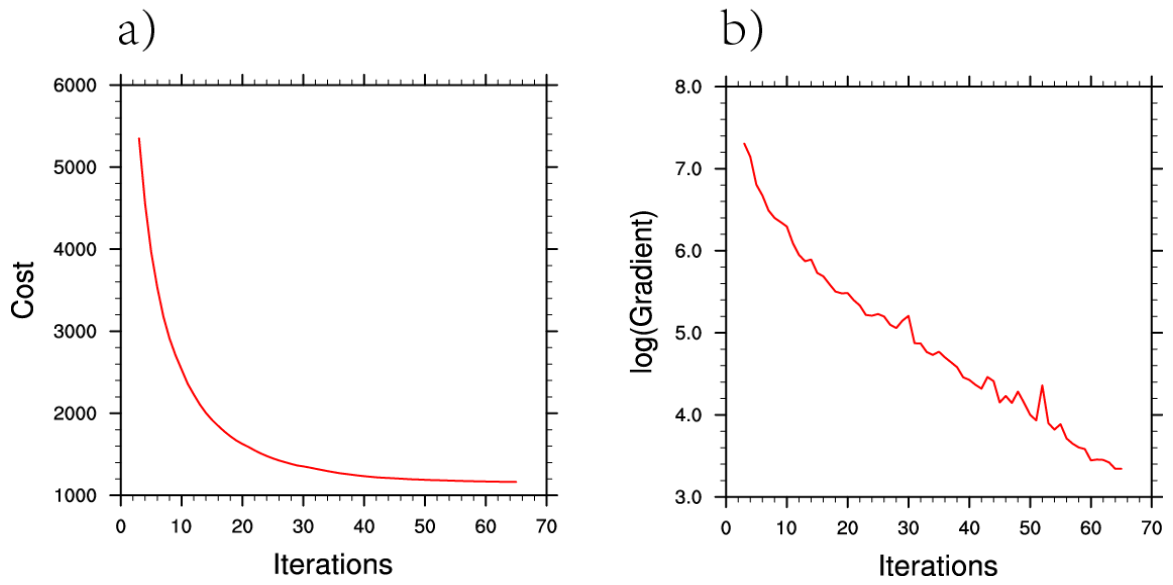
623

624

625

626

627



628

629 Fig. 6 (a) Cost function as functions of iterations, (b) gradient as functions of
630 iterations.

631

632

633

634

635

636

637

638

639

640

ch8(6.19 μ m)

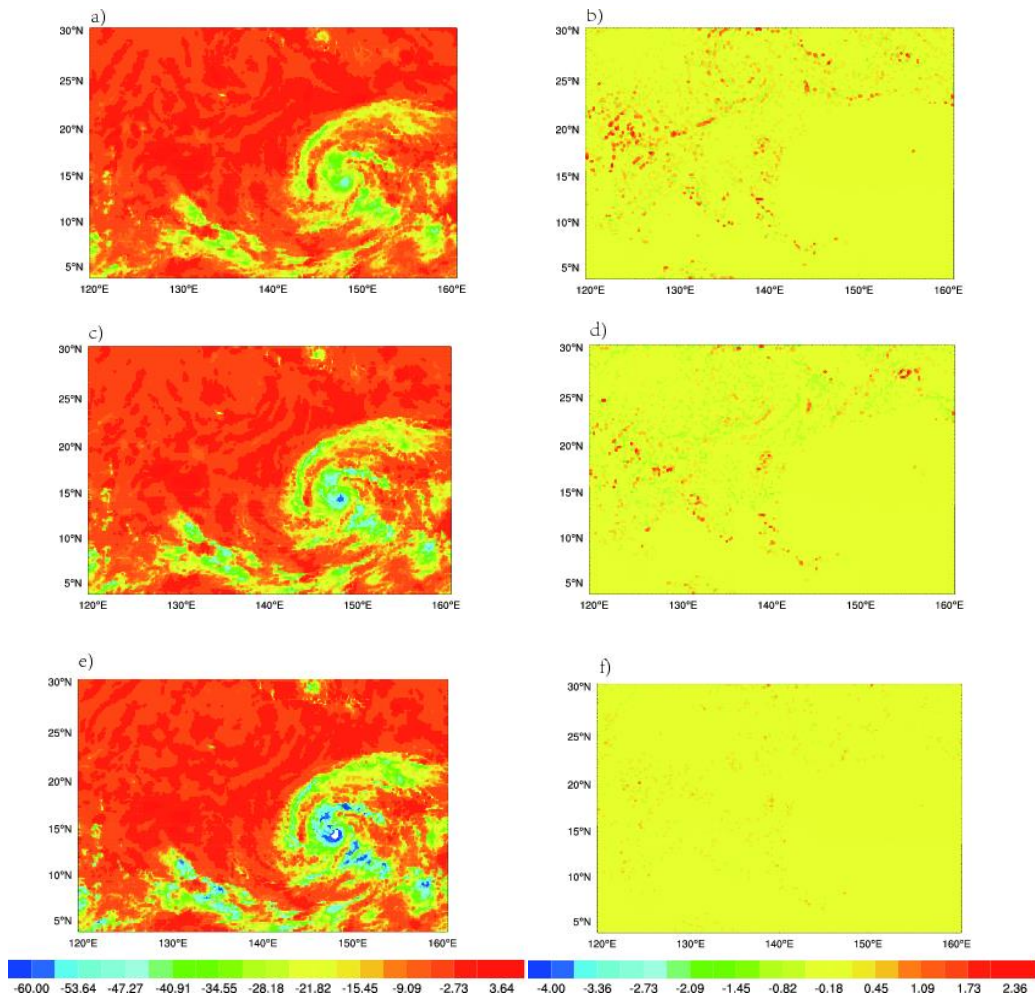
641

ch9(6.95 μ m)

642

ch10 (7.34 μ m)

643



644 Fig. 7 (a, c, and e) OMB (unit: K) after bias correction for channel 8, 9, and 10,

645 respectively; (b, d, and f) OMA (unit: K) after bias correction for channel 8, 9, and 10,

646 respectively at 0000 UTC 2 August 2015.

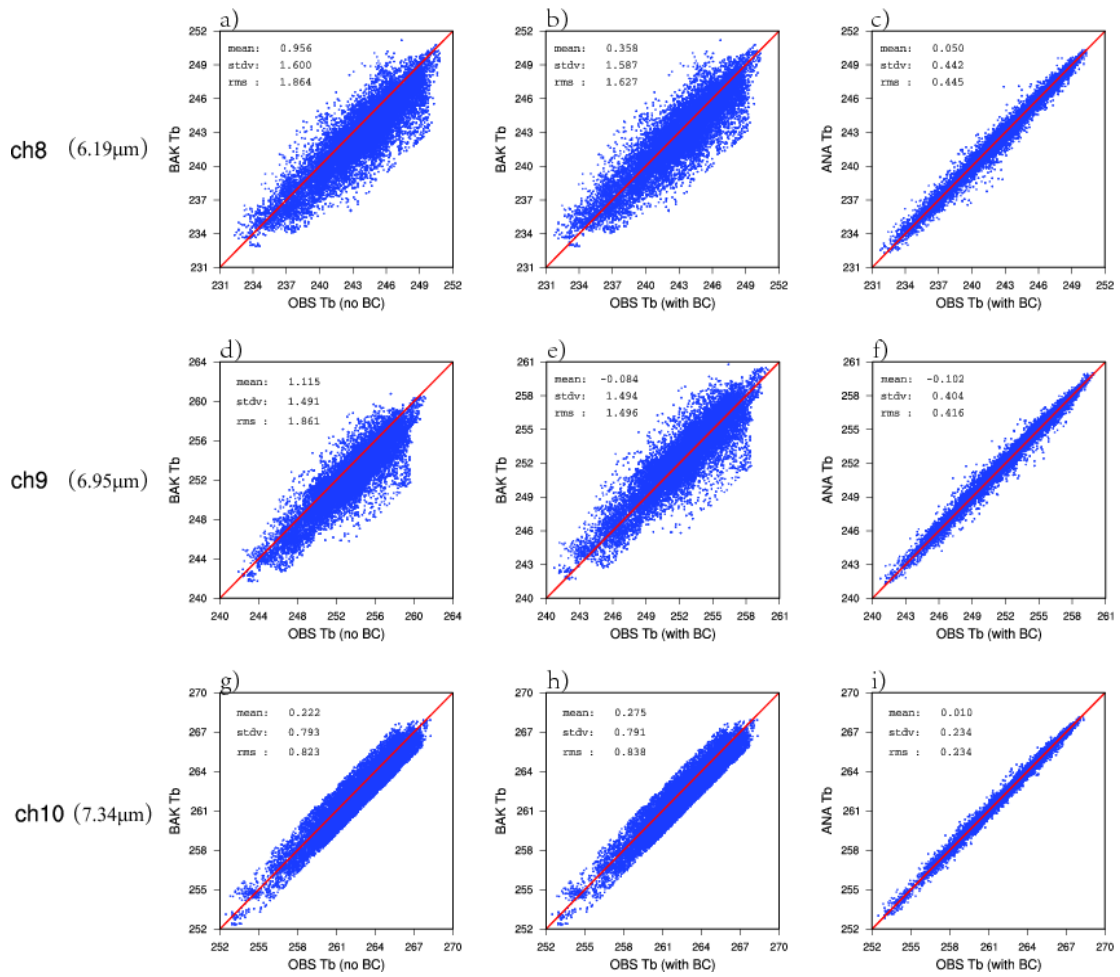
647

648

649

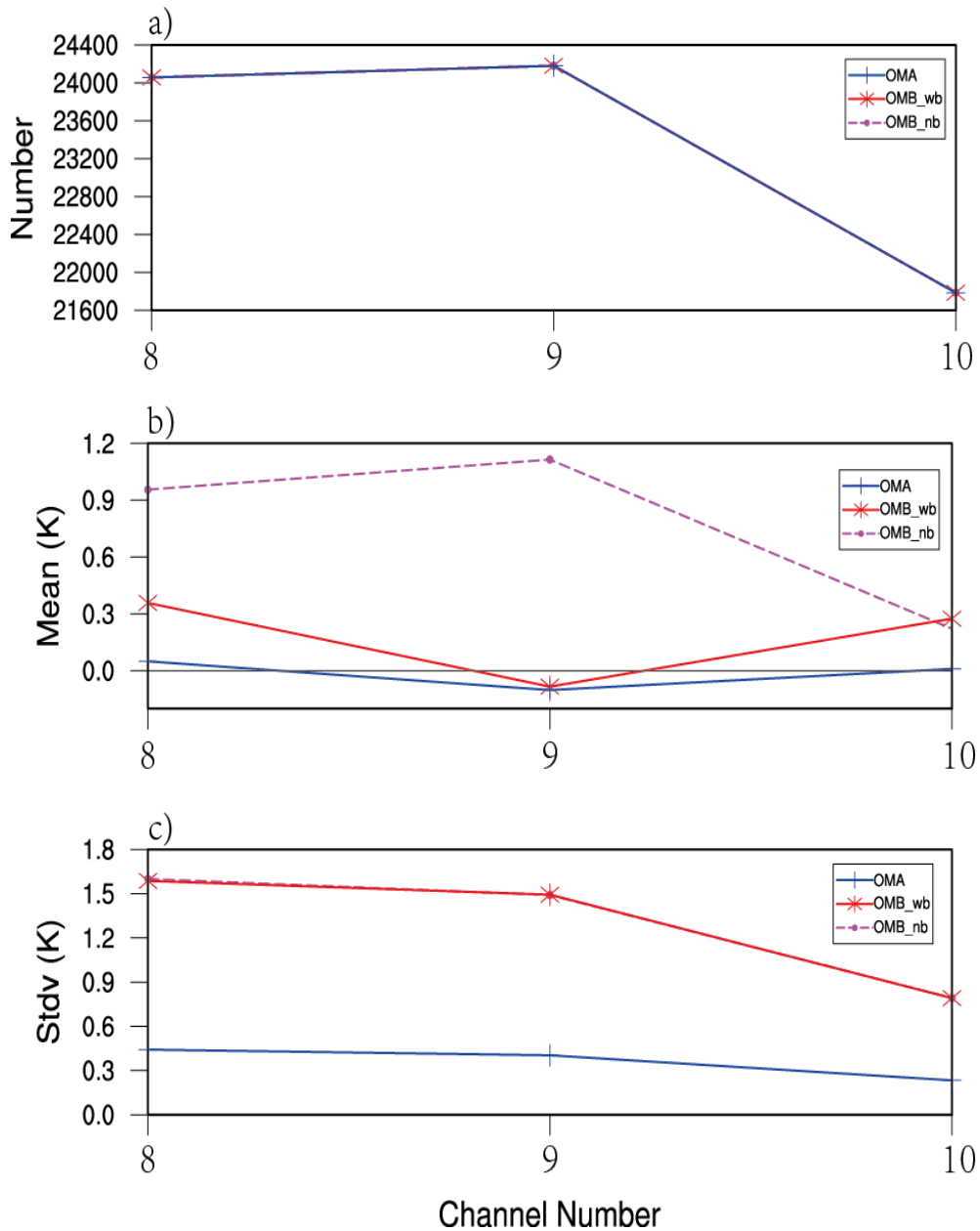
650

651



652

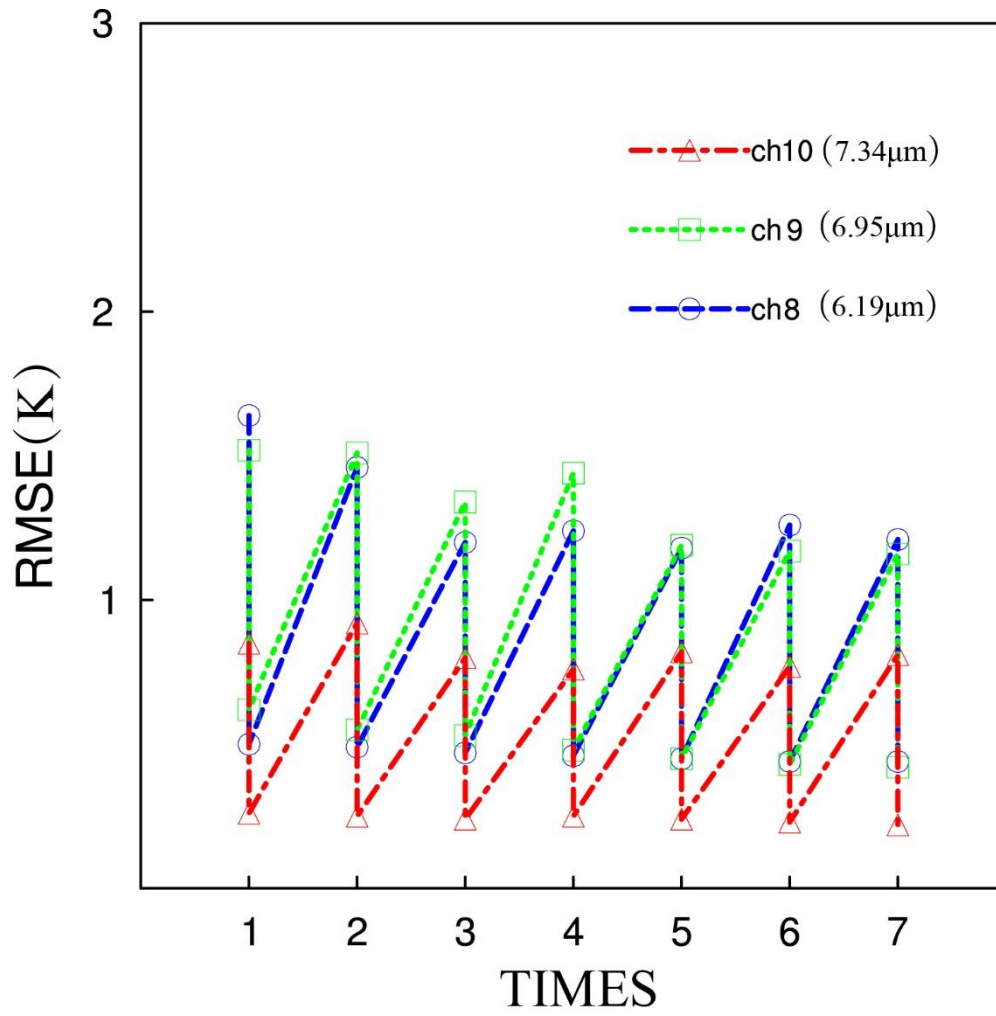
653 Fig. 8 Scatter plots of (a, d and g) the observed and background brightness
654 temperature before the bias correction of channel 8, 9 and 10. Scatter plots of (b, e
655 and h) the observed and background brightness temperature after the bias correction
656 of channel 8, 9 and 10. Scatter plots of (c, f and i) the observed and analyzed
657 brightness temperature after the bias correction of channel 8, 9 and 10.



658

659 Fig. 9 Number of (a) observations, (b) mean (unit: K), and (c) standard deviations
 660 (unit: K) of OMB and OMA before and after the bias correction for water vapor
 661 channels 8-10 (OMB_nb: OMB without bias correction; OMB_wb: OMB with bias
 662 correction).

663



664

665 Fig.10 Time series of the RMSE for the brightness temperature (unit: K) with
 666 assimilation times before and after the data assimilation.

667

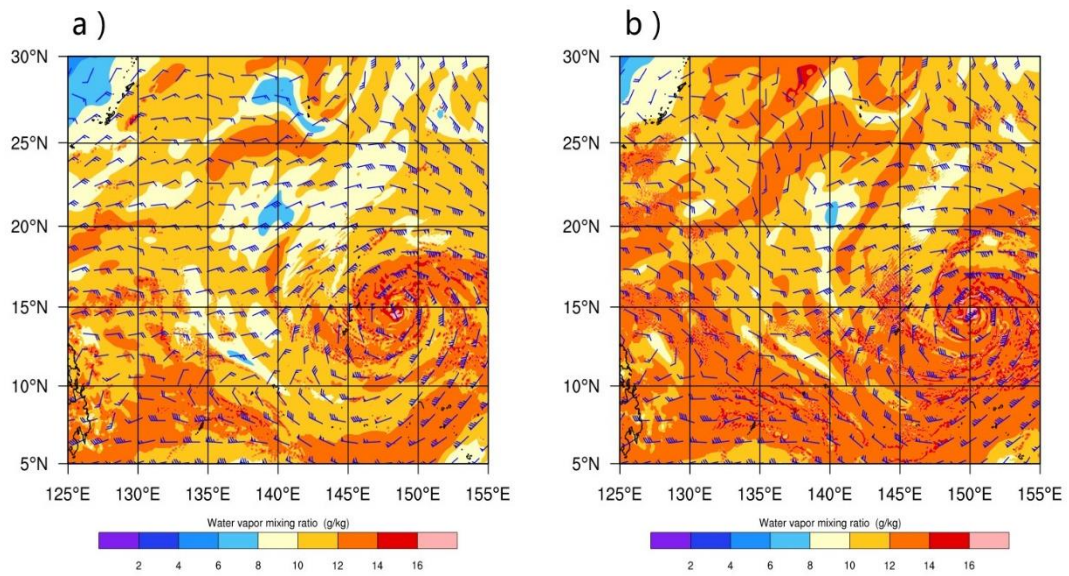
668

669

670

671

672



673

674 Fig. 11 The surface wind speed (vectors, unit: m s^{-1}) and water vapor (colored, unit:
675 g/kg) for (a) CTNL; (b) AHI_DA at 850 hPa at 0000 UTC 2 August 2015.

676

677

678

679

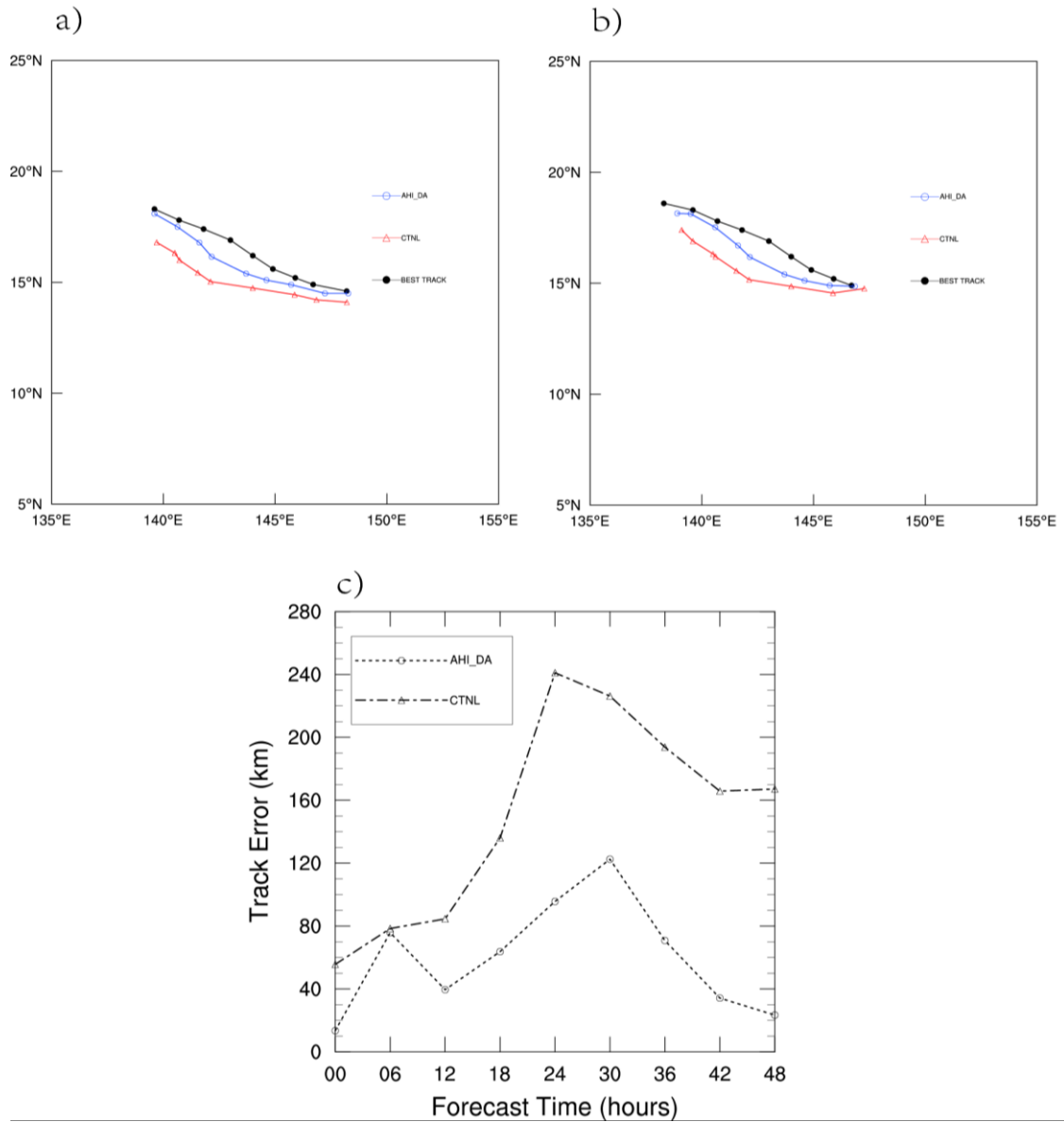
680

681

682

683

684



685

686

687 Fig. 12 The 48-hour predicted tracks (a) from 0000 UTC 2 August to 0000 UTC 4

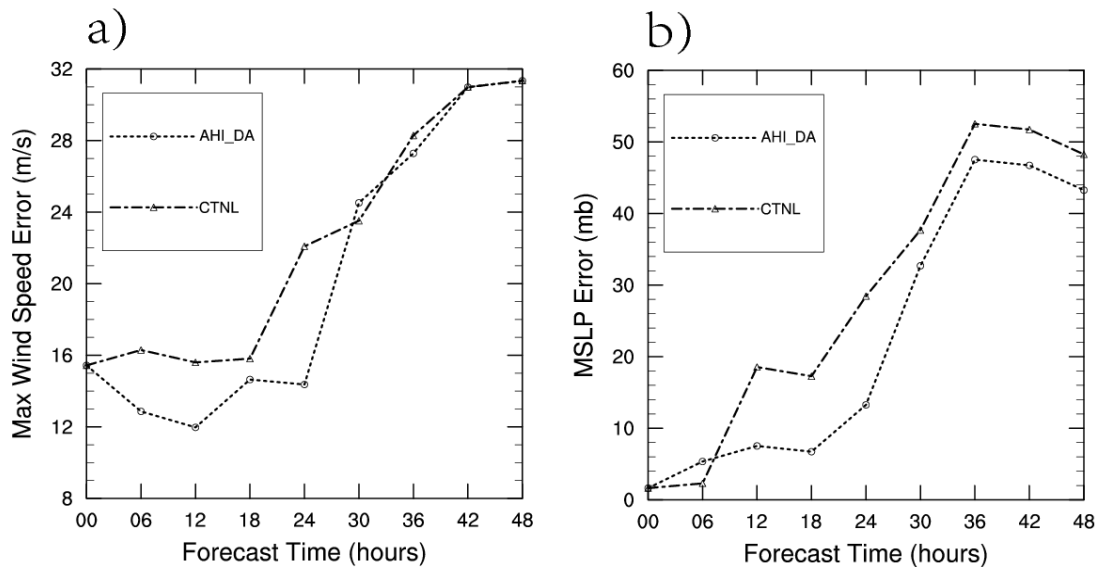
688 August, (b) from 0600 UTC 2 August to 0600 UTC 4 August 2015, (c) averaged track

689 errors (unit: m s^{-1}) for the two forecasts.

690

691

692



693

694 Fig.13 The 48-hour (a) maximum surface wind (unit: m s^{-1}), (b) minimum sea level
695 pressure (unit: hPa) of Soulder averaged from two forecasts.

696